Biosensors and Bioelectronics 219 (2023) 114772

Contents lists available at ScienceDirect

Biosensors and Bioelectronics

journal homepage: www.elsevier.com/locate/bios

A storm in a teacup -- A biomimetic lung microphysiological system in conjunction with a deep-learning algorithm to monitor lung pathological and inflammatory reactions

Zaozao Chen [a,c,1], Jie Huang [d,b,1], Jing Zhang [c,1], Zikang Xu [a], Qiwei Li [a], Jun Ouyang [c], Yuchuan Yan [c], Shiqi Sun [c], Huan Ye [c], Fei Wang [c], Jianfeng Zhu [c], Zhangyan Wang [b], Jie Chao [b,*], Yuepu Pu [b,**], Zhongze Gu [a,b,***]

[a] State Key Laboratory of Bioelectronics, School of Biological Science and Medical Engineering, Southeast University, SiPaiLou#2, Nanjing, Jiangsu, 210096, China
[b] Key Laboratory of Environmental Medicine Engineering, Ministry of Education, School of Public Health, Southeast University, Nanjing, 210000, China
[c] Institute of Biomaterials and Medical Devices, Southeast University, Suzhou, Jiangsu, 215163, China
[d] Department of Respiratory and Critical Care Medicine, Zhongda Hospital, Southeast University, Nanjing, 210009, China

ARTICLE INFO

Keywords:
Lung-on-a-chip
Microfluidics
COVID-19
Cytokine storm

ABSTRACT

Creating a biomimetic *in vitro* lung model to recapitulate the infection and inflammatory reactions has been an important but challenging task for biomedical researchers. The 2D based cell culture models – culturing of lung epithelium – have long existed but lack multiple key physiological conditions, such as the involvement of different types of immune cells and the creation of connected lung models to study viral or bacterial infection between different individuals. Pioneers in organ-on-a-chip research have developed lung alveoli-on-a-chip and connected two lung chips with direct tubing and flow. Although this model provides a powerful tool for lung alveolar disease modeling, it still lacks interactions among immune cells, such as macrophages and monocytes, and the mimic of air flow and aerosol transmission between lung-chips is missing. Here, we report the development of an improved human lung physiological system (Lung-MPS) with both alveolar and pulmonary bronchial chambers that permits the integration of multiple immune cells into the system. We observed amplified inflammatory signals through the dynamic interactions among macrophages, epithelium, endothelium, and circulating monocytes. Furthermore, an integrated microdroplet/aerosol transmission system was fabricated and employed to study the propagation of pseudovirus particles containing microdroplets in integrated Lung-MPSs. Finally, a deep-learning algorithm was developed to characterize the activation of cells in this Lung-MPS. This Lung-MPS could provide an improved and more biomimetic sensory system for the study of COVID-19 and other high-risk infectious lung diseases.

1. Introduction

Two-dimensional cell culture models and animal models have been developed for studies of airborne infectious diseases, such as COVID-19 and SARS (Bao et al., 2020; Chan et al., 2020; Yu et al., 2020). 2D cell culture technology has been used for a long time in the field of life sciences for the low cost, convenient preparation of seed cells, and full details of preliminary exploration. However, the 2D cell culture models are oversimplified in terms of cell-cell and cell-matrix interactions with the result that their application to understanding human lung infections has been limited. On the other hand, animal models, as the most widely used 3D models, are limited because of structural differences from the human lung and the manual labor involved in the preparation of lung samples needed to characterize the changes in lung structure caused by

* Corresponding author.
** Corresponding author.
*** Corresponding author. State Key Laboratory of Bioelectronics, School of Biological Science and Medical Engineering, Southeast University, SiPaiLou#2, Nanjing, Jiangsu, 210096, China.
E-mail addresses: chaojie@seu.edu.cn (J. Chao), yppu@seu.edu.cn (Y. Pu), gu@seu.edu.cn (Z. Gu).
[1] these authors contributed equally in this work.

https://doi.org/10.1016/j.bios.2022.114772
Received 17 June 2022; Received in revised form 7 September 2022; Accepted 28 September 2022
Available online 1 October 2022

infection. Moreover, this process can be dangerous if the animals exhibit serious infectious disease. Human tissue-based models have also been established. Chu et al. reported that human lung tissues harvested from surgery of lung cancer patients were used to study virus proliferation and inflammatory cytokine expression in lung tissues(Chu et al., 2020). Unfortunately, these tissues did not survive long *in vitro*, and during surgery and sample preparation, immune cells inside the lung tissue were largely lost.

In human organs-on-a-chip (OOC) systems or human microphysiological systems (hMPSs), functional miniature human organs are constructed using microfabrication and tissue-engineering techniques (Zheng et al., 2016). hMPSs create a biomimetic microenvironment for the continuous culture of these miniature organs with optimized tissue structure and cell composition similar to that in the corresponding human organs (Sunghee Estelle Park, 2019). OOCs and MPSs have now been commonly used for evaluating the effectiveness and toxicity of drugs to reduce the usage of animals (Huh et al., 2012b; Low et al., 2021; Low and Tagle, 2017; Mehta et al., 2012). In 2010, the Ingber lab in the Weiss Institute created a lung OOC model to simulate the alveoli structure and its contraction and relaxation (Huh et al., 2010). Recent applications of this model include the detection of bacteria, chemicals, nanoparticles and other harmful materials (Huh et al., 2012a; Si et al. 2021a, 2021b). Our group also developed multiple MPSs, including an inverse opal-like hydrogel-based lung MPS, and utilized a deep learning-based model for tissues in organs-on-a-chip analysis(Chen et al., 2021; Huang et al., 2021; Yang et al., 2021; Zheng et al., 2016).

SARS-CoV-2, the virus that causes COVID-19, enters cells by attaching to ACE2 receptors followed by endocytosis. ACE2 receptors are widely expressed in various cells of the human body, although their expression in alveolar epithelial type II cells is higher than that in other organs of the human body, including the intestinal tract, liver and vascular endothelia (Jing et al., 2020; Pal and Bhansali, 2020; Pirola and Sookoian, 2020; South et al., 2020). The lethality of COVID-19 is higher than that of common influenza, and the cause of death in infected individuals is associated with cytokine storms (Chan et al., 2020; Chu et al., 2020). Autopsy results showed that COVID-19 patients produced large amounts of mucus in the lung bronchi and had damaged alveolar cells with mucus on their surfaces; it was suspected that the mucus was produced by the bronchial epithelia and infiltrated into the alveoli (Chan et al., 2020; Chu et al., 2020). Therefore, to construct a lung-on-a-chip (LOC) model for COVID-19, a chip containing cells expressing ACE2 receptors is needed, and not only an alveolar structure but also a lung bronchus structure needs to be constructed. To simulate the inflammatory cascade that occurs inside of the lungs of COVID-19 patients, immune cells to simulate resident macrophages existing in alveolar interstices and circulating leukocytes should also be introduced (Chu et al., 2020).

In this study, we constructed a human lung physiological system (Lung-MPS), consisting of bronchial components and alveolar components, resident macrophages, and circulating monocytes. The chip material, flow control, pumps option are important in physiological systems like the MPS(Danku et al., 2022), in consideration of the biocompatibility and drug absorption, we choose poly (methyl methacrylate) (PMMA) as the raw chip material to fit a peristaltic pump system. The integration of multiple immune cells in the lung MPS has enabled us to monitor the amplification of inflammatory signals in the system. A deep-learning-based recognition module was included in this system to evaluate and classify the inflammation-induced changes in epithelium and macrophage morphology. We also constructed a fully automated spreading system that was capable of simulating droplet spreading in a typical human-human infection process. Liquid supply, culture devices, and other components were all integrated into a system to conduct viral studies with minimal risks. Using this setup, we investigated the spreading of spike protein and pseudoviruses in the LOC model and explored measures to reduce the spread of these pathogens.

2. Materials and Methods

2.1. Cell culture

The lung epithelial cell lines, including BEAS-2B,NCI-H441,A549, Calu-3,the human monocytic cell line THP-1,the human endothelial cell line HUVEC,were all purchased from the Global Bioresource Center (ATCC) and cultured according cell-culturing protocols. The details were shown in supporting information (Methods.S1).

2.2. Design and fabrication of Lung-MPS micro-device

The Lung-MPS device fabricated by CNC technology contains a poly (methyl methacrylate)(PMMA) chip body and a plug-in connector. The PMMA chip body is comprised of four PMMA layers and a porous membrane layer. The four PMMA layers consist of an upper connection layer, an upper cell culture layer, a lower cell culture layer and a lower seal layer. The upper connection layer is used for plug-in connector connection and it has two pores for adding cells into the chip. Both the upper and lower cell culture layer contain one or two (to simulate pulmonary bronchi and alveoli individually) cell culture unit and microchannels. The microchannels are 0.4 mm high and 1 mm wide. The sizes of the cell culture units are 7 mm long, 2 mm wide and 0.4 mm high. The upper cell culture unit and lower cell culture unit are separated by a track-etched polyethylene terephthalate (PET) membrane (ipCellCulture, it4ip, Belgium) containing 0.45 μm diameter circular pores. All the PMMA layers were cleaned using ethyl alcohol and deionized water. Then the PMMA layers and the porous membrane were combined into an integrated chip body with biocompatible double-side adhesive as is shown in Fig. 1A I. The upper two PMMA layers were first combined with a medical grade pressure-sensitive adhesive (ARcare 90445Q, Adhesives Research) into a whole upper unit. The lower two PMMA layers were then combined with the same medical grade pressure-sensitive adhesive into a whole lower unit. The upper and lower edge surface of the porous membrane were combined to the upper unit and the lower unit with the grade pressure-sensitive adhesive individually. A polytetrafluoroethylene (PTFE) membrane with 0.2 mm pore size was cut into proper size and bonded to the chip using double-sided pressure sensitive adhesive for bubble removal. The User-friendly plug-in connector was inspired from video graphics array (VGA) interface. The operation of the connector is convenient and simple. It just needs to insert the connector into the chip and tightened through the two screws on the side of the PMMA base. All the fluids loading and perfusion were controlled by a homemade fluid control system which was driven by peristaltic pumps. The detail was referenced in Supplementary Fig. S5, the holder could mostly accommodate 4 chips which could be perfused by 2 pumps (6-channel Pump, Takasago Fluidic Systems), and the controller was designed to set perfusion speed, time of each channel. The flow speed could adjust belong 1 μL/min to 1000 μL/min which is enough to obtain an appropriate fluid flow to mimic the microenvironment but without a harmful shear stress.

2.3. Lung-MPS micro-device simulates the model of disease transmission

We used two sets of chips in Lung-MPS – one set represents upstream "infectious" lung-chip and one set represents downstream normal lung chip, and a nebulizer to mimic the disease transmission. The system is shown in Fig. 4. The upstream chip simulates an infectious person, while the downstream chip simulates a normal person. Nebulizer receives virus from the infected chip and transmits the virus to the normal chip to simulate a person-to-person process. The virus in the upper cell culture unit of infectious chip is conveyed out of the chip by a peristaltic pump and flows into a nebulizer, in which it is nebulized into spray. A surgical mask insert was added to examine if the mask could prevent virus transmission.

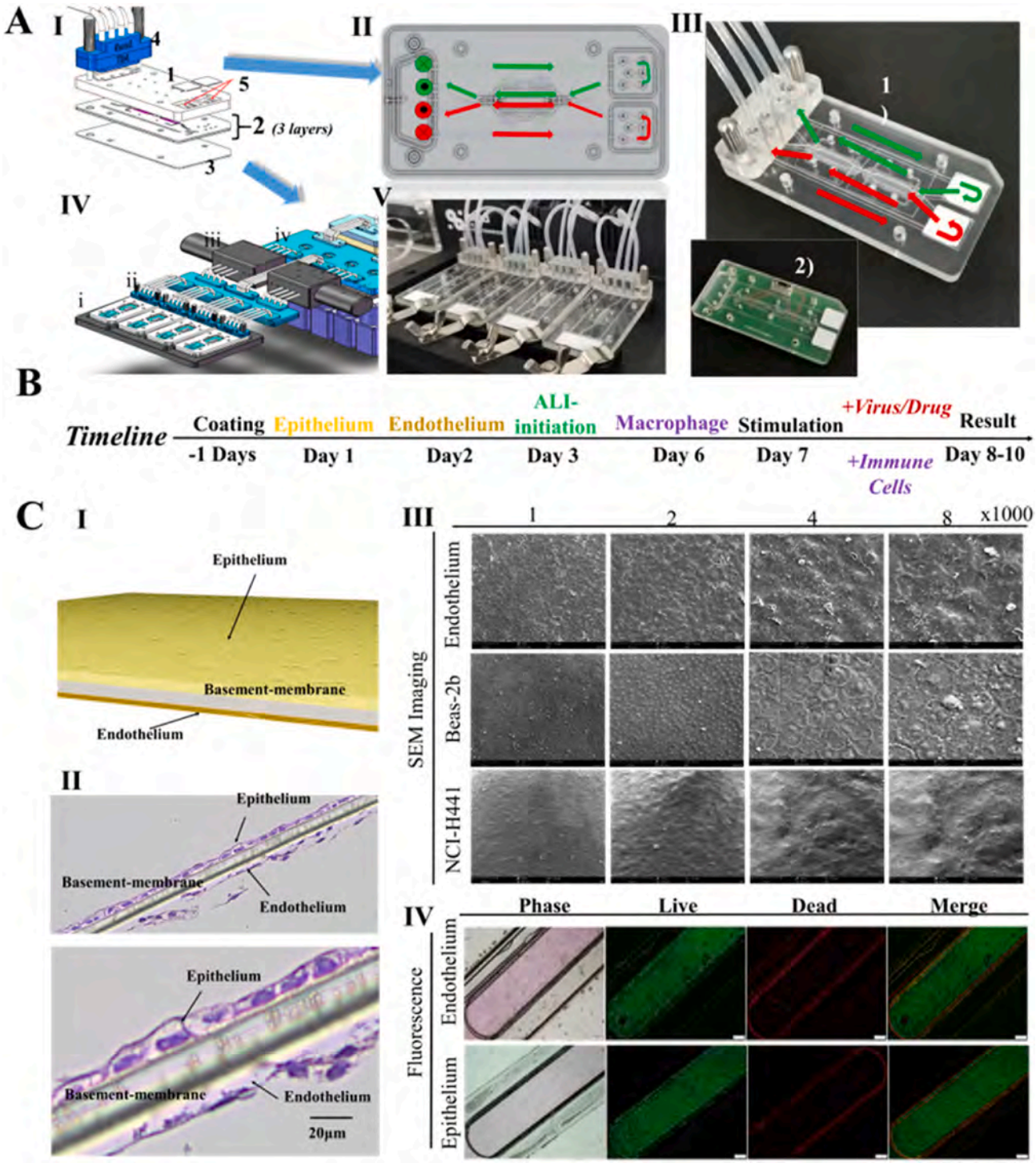

Fig. 1. Design and Construction of a Lung Microphysiological System. A) The appearance of the Lung-MPS chip. (I) The overall view of the Lung-MPS chip (1) the top layer of the chip; (2) the middle layer containing channels and sub-chambers for epithelium (bronchial and alveolar) and endothelium culture; (3) the bottom layer of the chip; (4) the VGA-like microfluidic connector for perfusion; (5) bubble trap and bubble filter structure. (II) Top view illustration of the flow in Lung-MPS chip. (III) Photograph of actual Lung-MPS chip. 1) green and red indicate the flow direction in upper and lower chambers or channels individually. 2) the appearance of the Lung-MPS chip with TEER detection electrodes. (V) The perfusion system has a pumping head that can simultaneously control up to four LOC. (IV) Schematic of the perfusion system: i to iv are the lung-chip, connectors and tubing, the peristaltic pump and pump head and the scaffold for the flow system, respectively.B) A typical timeline for construction of the Lung-MPS. C) The epithelium and endothelium morphological analysis. (I) Schematic illustration of lung epithelium(BEAS2b) and endothelium(HUVEC) on the Transwell-like membrane in the Lung-MPS. (II) Cryosectioning and H&E staining of Lung-MPSs showing the presence of epithelium and endothelium on both sides of the membrane at lower (top) and higher (bottom) magnification(Day 5). (III) Scanning electron microscopy (SEM) image showing endothelium and epithelium growth on the membrane(Day 5). (IV) Live/dead staining of the endothelium and epithelium in the chip chambers, showing the high viability of cells in the Lung-MPS(Day 7).

2.4. Generation of pulmonary bronchi and alveoli

The culture process is comprised of four main phases: the culture of human pulmonary bronchial epithelial cells and alveolar epithelial cells, the submerged culture of human endothelial cells, the subsequent culture at the air-liquid interface (ALI), and an additional co-culture of macrophages with epithelial cells. The details were shown in supporting information (Methods.S2).

2.5. Inflammatory stimulation

The upper chambers of the Lung-MPSs were treated with 10 μg/mL LPS in 50:50 mixtures of complete DMEM and RPMI-1640 medium flowing for 24 h. Meanwhile, the lower chambers were flowed with control medium or THP-1 cells in 50:50 mixtures of complete DMEM and RPMI-1640 medium. After stimulation, the effluent of the upper chambers was collected for chemokines and cytokines (IL-6, TNF-α and MCP-1) detection using ELISA kits (Proteintech, USA), and the devices were reserved for further characterization.

2.6. SARS-CoV2 spike protein and pseudo-virus infection

The details of SARS-CoV2 spike protein incubation and pseudovirus infection were shown in supporting information (Methods.S3).

2.7. Inflammatory response

2.7.1. Monocyte adhesion

The endothelial layer was live-stained for 30min at 37°C using Hoechst 33342. THP-1 cells were labeled with CMTPX (1 μM) for 1 h before being used. After microfluidic device was treated with LPS (10 μg/ml) for 24 h, the monocytes (5×10^5 cell/mL) were perfused in microfluidic device at a speed of 0.1 mL/min for 30mintutes. The movies were taken using time-lapse function of OCRA-Spark CMOS (Hamamatsu, Japan). The micrographs of four or five random areas were taken using an IX-83 microscope and cell counting quantification was carried out by counting attached monocyte using ImageJ software. For monocyte adhesion assays, the epithelial cells were seeded in the lower chambers while the endothelial cells were cultured in the upper chambers to avoid the affection of gravity.

2.8. Epithelium and endothelium morphological analysis

2.8.1. Cell viability

Cell viability was carried out by live/dead cell staining (Thermo Fisher Scientific, USA). The microfluidic device was slightly washed three times with DPBS, then incubated with 60ul dye at 37°C for 30 min and observed on an IX-83 microscope.

2.8.2. Histological and immunofluorescence staining

The culture membranes of the Lung-MPSs were carefully separated from the devices by cutting along the equivalents' edge with a scalpel, fixed in 10% neutral buffered formalin and embedded into paraffin. Deparaffinized sections of 5 μm were transferred onto slides for hematoxylin-eosin (HE) staining. The bright-field images of HE staining were acquired for general analysis of the pulmonary equivalents' morphological architecture. Caseviewer software was used to measure histological features.For immunofluorescence staining, the details were shown in supporting information (Methods.S4).

2.8.3. Scanning electron microscopy

For micromorphology observation, the excised membranes of the Lung-MPSs were fixed in cold 4% paraformaldehyde for 2h for scanning electron microscopy (SEM) detection. Before observation, the membranes were rinsed in PBS, then dehydrated through gradient ethanol solutions from 25 to 100% and incubated for up to 10 min in each interval. Samples were air-dried overnight in a desiccator at room temperature, mounted using conductive adhesive tabs and coated with a thin layer of gold under vacuum for scanning electron microscopic imaging with a Phenom Pro scanning electron microscope (Phenom pro, Netherlands).

2.9. Barrier function assays

2.9.1. Transepithelial electrical resistance (TEER) assays

The electrical resistance of these Lung-MPSs in different treatment conditions were measured using EVOM2 (World Precision Instruments, USA) to investigate the barrier function. For immunofluorescence staining, the details were shown in supporting information (Methods. S5).

2.9.2. Paracellular permeation

To examine the permeability, the Lung-MPSs were perfused with 607 Da Cascade blue solution (50 μM), and detected at 4 h. For immunofluorescence staining, the details were shown in supporting information (Methods.S5).

2.10. Deep-learning algorithm for inflammation classification

2.10.1. Setup

Firstly, we captured 200 bright field cell images in different categories (LPS and Control), respectively. Then, we splited the whole dataset into train and test set with a ratio of 7:3. We used train set to fine-tune the pretrained VGG-19 network and evaluated inflammation classification accuracy on test set.

2.10.2. Image pre-processing and patch extraction

Each brightfield image was converted into a gray-scale image to avoid the impact of hue and saturation and minimize the effects of different imaging conditions. The image was then normalized to a standardized intensity ranging [0,1]. Next, a 224×224 sliding-window with an overlap of 25% was used to extract patches from gray-scale images. After patch extraction, we got 32,000 image patches, which is basically enough for network fine-tuning. At training stage, we used Torchvision Library(Marcel and Rodriguez, 2010) to augment the train set by randomly horizontally and vertically flipping and randomly rotation with a probability of 0.5, 0.5 and 0.25, respectively.

2.10.3. VGG-19 architecture

We used VGG-19 Network to obtain different scale features through composed convolution groups, and then used fully connected layers as a classifier to distinguish different categories. VGG19 is the name of a neural network that was proposed by Visual Geometry Group in Oxford University in the paper "Very Deep Convolutional Networks for Large-Scale Image Recognition (ICLR, 2015)"(Simonyan and Zisserman, 2015), when a series of network architecture contains VGG11, VGG13, VGG16, VGG19, which are named by the number of weight layers in their model. These networks aim to solve the image classification task using artificial intelligence. In our paper, we choose the VGG19 architecture for classification. In the VGG-19 model, we used a combination of convolution blocks with different feature channels and fully connected blocks, to implement an end-to-end method for accurate image classification. The convolution block consists of 16 convolutional layers and 4 max-pooling layers, with the convolutional kernel set as 3×3. The fully connected block consists of 3 fully connected layers. The result of the network input of 224×224 corresponds to an output of 1×2, which is the probability of a certain category.

2.10.3.1. Transfer learning on bright field image dataset. Due to the small number of images in our bright field image dataset, the proposed VGG-19 model was pre-trained on ImageNet to optimize parameters in

convolution blocks for feature extraction. By pre-training the model on ImageNet, more useful high-level features can be attracted for image classification. Then, the parameters in convolution blocks are frozen and the network is retrained on our dataset to optimize the parameters in fully connected layers. We also trained VGG-19 model only using our bright field image dataset from scractch, while the prediction accuracy is significantly lower than that of using pretrained model.

2.10.3.2. Inflammation classification. Acquired bright field cell images in different categories (LPS and Control) were processed using the network model to obtain the classification results. The computer hardware is Core i7-9700K @ 3.60 GHz CPU on Z390 UD main board with 32 GB(DDR4,2666 MHz) RAM, 860 EVO 500 GB SSD Hard Disk, Nvidia GeForce RTX 2080 Ti (11 GB) Graphics Card, and DEL40E8 DELL U2417H monitor. VGG-19 Algorithm took less than 0.5s to classify the label of a single image (Image resolution at 1200 × 980 × 3, size ~300 KB).

2.11. Statistical analysis

Data was expressed as mean ± SEM. Statistically significant difference was determined by either Student t-tests or one-way ANOVA and Tukey's post hoc test, statistical significance was set at $p < 0.05$.

3. Results

3.1. Construction of a lung-on-a-chip system

To precisely simulate the lung, we constructed a lung microphysiological system with an alveolar chamber and a bronchial chamber, as shown in Fig. 1A. Each chamber was divided into two separate spaces by a porous membrane; the upper chamber was used for culturing bronchial or pulmonary epithelial cells, and the lower chamber was used for culturing pulmonary vascular endothelial cells. Loading ports facilitated communication between the upper and lower chambers and can be used for injection of extracellular matrices (ECM), loading and reloading of cells, adding drugs or inhibitors, and sampling the medium for further analysis or measurement of electrical impedance in the system. We designed a multichannel connector (Fig. 1A I4) for perfusion of the upper and lower chambers independently. We manufactured a kit with all required reagents and equipment (Supplementary Fig. S1), including culture medium, detection reagents, chip bodies, tubing, and other accessories. Operating procedures for the addition of ECM, cells, and subsequent culture and perfusion are described in the Materials and Methods. In brief, a bronchi structure was constructed using bronchial epithelial cells, Beas-2B; the alveolar epithelial structure was constructed using type II pneumocyte-like epithelial cells, NCI-H441, and the vessel chambers consisted of human umbilical vein endothelial cells, HUVECs. H&E staining, fluorescent-based live/dead staining and scanning electron microscopy (SEM) images demonstrated the formation of a dense epithelial layer (Fig. 1C I-IV). After one week of cell culture both the epithelial and endothelial layers maintained high viability (>95%).

3.2. Simulation of the inflammatory cascade reaction in the in vitro lung-on-a-chip system

The inflammatory cascade reaction is generally used to describe the amplification of an inflammatory reaction. For example, macrophages can "sense" immunogenic substances, such as PAMPs (pathogen-associated molecular patterns), or DAMPs (damage-associated molecular patterns)(Denning et al., 2019; Takeuchi and Akira, 2010), and secrete inflammatory cytokines, thereby inducing activation of endothelial cells and triggering adhesion and aggregation of many monocytes on the endothelial layer (Supplementary Fig. S2A). To introduce the key component in inflammatory reaction, we built a perfusion system to deploy residential macrophages and later the circulating monocytes into the lung-MPS. The perfusion system is shown schematically in Fig. 1A IV and the chips connected in the perfusion system are shown in Fig. 1A V.

We first introduced macrophages into the system on Day 6. The ratio of macrophages to epithelial cells is 1:10, similar to that found in humans(Stone et al., 1992). Macrophages adhered to the surfaces of the epithelial cells were imaged by H&E staining or SEM (Fig. 2A). The alveolar epithelia, endothelia and macrophages in the model system have a barrier function as shown by trans-epithelial electrical resistance (TEER) measurements of the components alone and of the composite structure on Day 8 after construction of the system (Supplementary Fig. S3). The TEER value of the combined epithelial and endothelial layers was greater than that of either layer alone. Adding macrophages to the induced model reduced the TEER value, suggesting a potential effect of immune cells on lung permeability. To study the inflammatory cascade reaction, we also introduced circulating monocytes into the lung-MPS system containing the macrophages. We added 10 μg/ml LPS to activate macrophages in the chip. By continuous monitoring of flowing monocytes in the chip with the pumping system, a great number of leukocytes adhering to the endothelial layer were observed after LPS stimulation (Fig. 2B–E, Supplementary Movie S1).

Supplementary data related to this article can be found at https://doi.org/10.1016/j.bios.2022.114772.

With circulating monocytes, the expression of inflammatory factors, including TNF-α, IL6 and MCP1, increased over 8-fold compared with systems w/o circulating monocytes, indicating an enhanced inflammatory response with the perfusion system (Fig. 3A, I-III). Concomitantly, the inflammatory reaction caused more significant decreases in the TEER values with the circulation of monocytes (Fig. 3B), indicating that the tri-culture of macrophages and monocytes with either bronchial or alveolar epithelial cells can aggravate inflammation. An increase in mucus secretion was also observed in alveolar chambers stimulated with LPS (Supplementary Fig. S4).

3.3. Lung microphysiological system model for droplet spreading simulation

Droplet spreading through speaking, breathing, and coughing are typical spreading modes for airborne diseases. To construct an *in vitro* model capable of simulating droplet spreading, we designed and constructed an integrated system containing upstream lung-MPSs, nebulizers, protective masks, downstream lung-MPSs and other accessories, including pumps and controllers (Fig. 4A). The left arm of the system is the upstream lung-MPSs, which contains 4 chips, a pumping subsystem and a controller. Using culture fluid in the alveolar epithelia chamber, a defined volume (500 μl) was automated pumped into a nebulizer (Materials and Methods) to generate fluid droplets and/or aerosols with an average size of 3.9 ± 25%, and >65% of particles were smaller than 5 μm (Materials and Methods). The droplets were then guided and harvested, followed by pumping into downstream Lung-MPSs. The workflow (time and speed) of each pump was programmed, and the operation was fully automated (Fig. 4B, Supplementary Fig. S5).

To detect droplet generation and measure spreading efficiency, we used food colorants and fluorescent microbeads to visualize the diffusion of small molecules or substances from the upstream Lung-MPSs to the downstream Lung-MPSs (Fig. 5A). The droplet generator was operated for 20 s and the medium in upstream Lung-MPSs that contained pigments at a concentration of 5 mg/mL formed droplets and entered the medium in downstream Lung-MPSs diluted ~20-fold, as determined by a colorimetric measurement. This experiment was repeated using 1 μm fluorescent microbeads with the result that the microbeads were approximately 16-fold diluted when they arrived downstream.

To test the spreading model and its blockage with protective measures, we also examined the influence of protection equipment (surgical masks) on the spreading of the specimen. The masked group reduced the number of both food colorants and microbeads to <5%, suggesting a

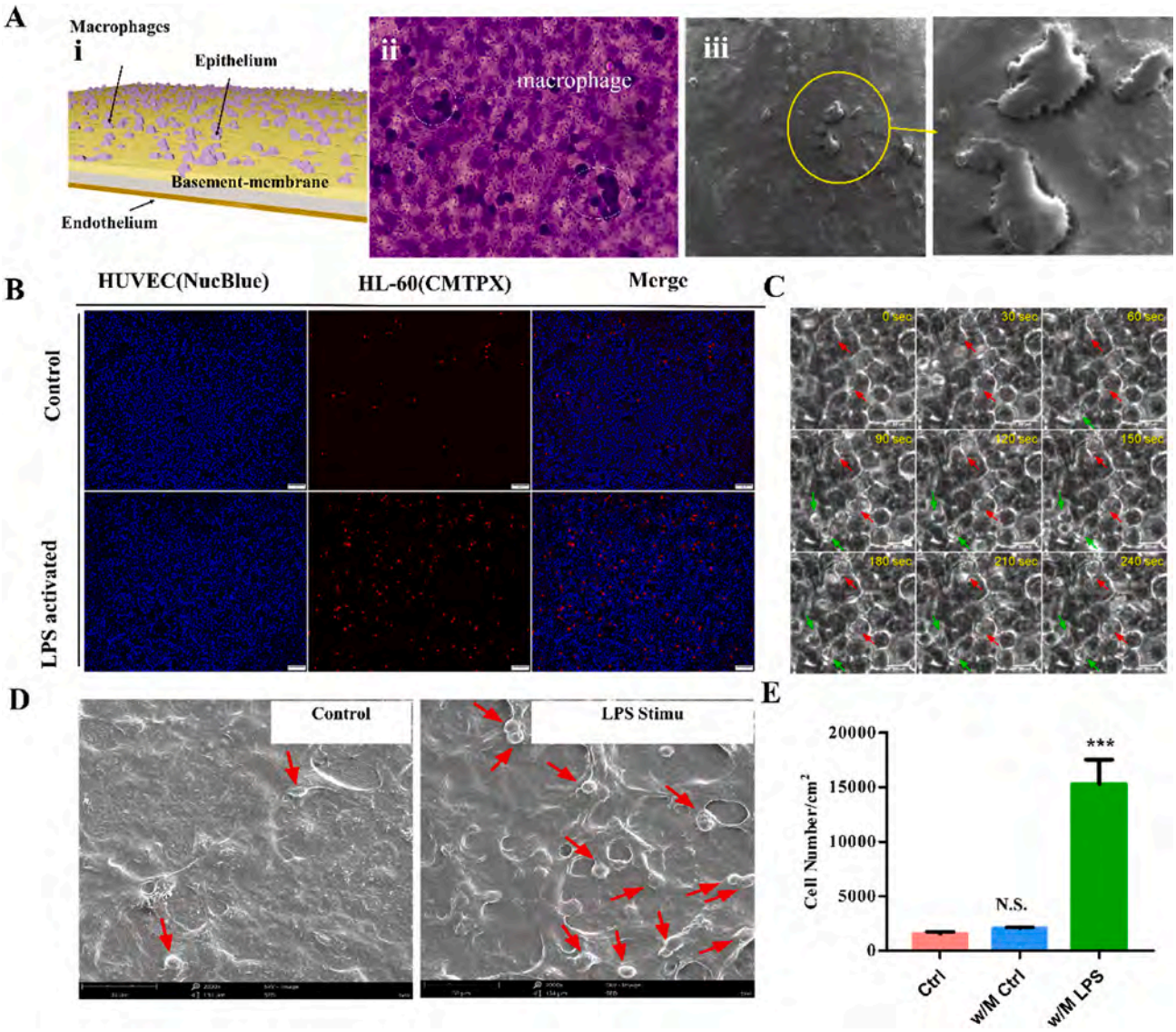

Fig. 2. Introduction of Immune Cells in the Lung-MPS to Simulate Early Inflammation. A) Seeding of macrophages on an epithelial layer. i) Schematic drawing, ii), H&E staining, iii) SEM imaging, showing the presence of macrophages on lung epithelium. B) Monocytes attached to the endothelium w/or w/o LPS treatment (10 μg/ml) during perfusion. Endothelial cells were labeled with NucBlue for the nucleus (blue), and monocytes were stained with cell tracker red (red). Scale bar, 200 μm. C) Frames from a movie showing the rolling and gradual adhesion of monocytes attached to the endothelium in Lung-MPSs pretreated with LPS. Red arrows point to preexisting monocytes on the endothelium, and green arrows indicate new monocyte attachment. Scale bar, 20 μm. D) SEM images showing monocyte attachment to the endothelium with or without LPS treatment. E) Quantitative comparison of monocyte adhesion on the endothelium in the Lung-MPS w/or w/o LPS group. Significance was calculated by one-way ANOVA with Tukey's post-hoc tests. *$p < 0.05$, ***$p < 0.001$. N.S., no significance.

preventive effect of protective masks on the spreading of particles, compared with a nonmask group (Fig. 5A-I and II).

3.4. *Application of Lung-MPS for the study of SARS-CoV-2 spike protein and pseudovirus infection*

We explored whether our Lung-MPS system could be useful in the study of lung-related infectious diseases using SARS-CoV-2 mimetic spike protein or SARS-CoV-2 pseudovirus (Materials and Methods). All virus experiments were carried out in a BSL-2 laboratory. Briefly, the epithelium chamber in air-liquid culture was filled with medium for 10 min before spike protein attachment or the pseudovirus infection experiment, and spike protein (250 ng/mL) or pseudoviruses (10^7IU/ml) were added to the upstream buffer tube and flowed through the epithelium chamber of the upstream Lung-MPSs for 24 h. The solution in the buffer tube was also pumped into the upstream reservoir before the nebulizer and atomized. The atomized mists with or without mask blockage were harvested by the downstream reservoir and then pumped into downstream Lung-MPSs. The epithelium chamber in both upstream and downstream Lung-MPSs was washed and kept in air-liquid culture for another 24 h before fixation with 4% paraformaldehyde. Immunocytochemical staining was performed for analysis of the spike protein experiment. Colocalization of ACE2 and spike protein was observed in over 70% in BEAS-2B and NCI-H441 cells (Fig. 5B, Supplementary Fig. S6). For the virus experiment, the percentage of cells transduced (Fig. 5C) with pseudoviruses was monitored for GFP expression in the cytoplasm. We observed the transportation of pseudoviruses from the upstream Lung-MPSs to the downstream Lung-MPSs. The mask blocked almost all pseudovirus infections, which indicated the usefulness and effectiveness of the protective measures. Taken together, both the spike protein and the pseudovirus experiment demonstrated the potential of this Lung-MPSs for the study of infection by airborne pathogens.

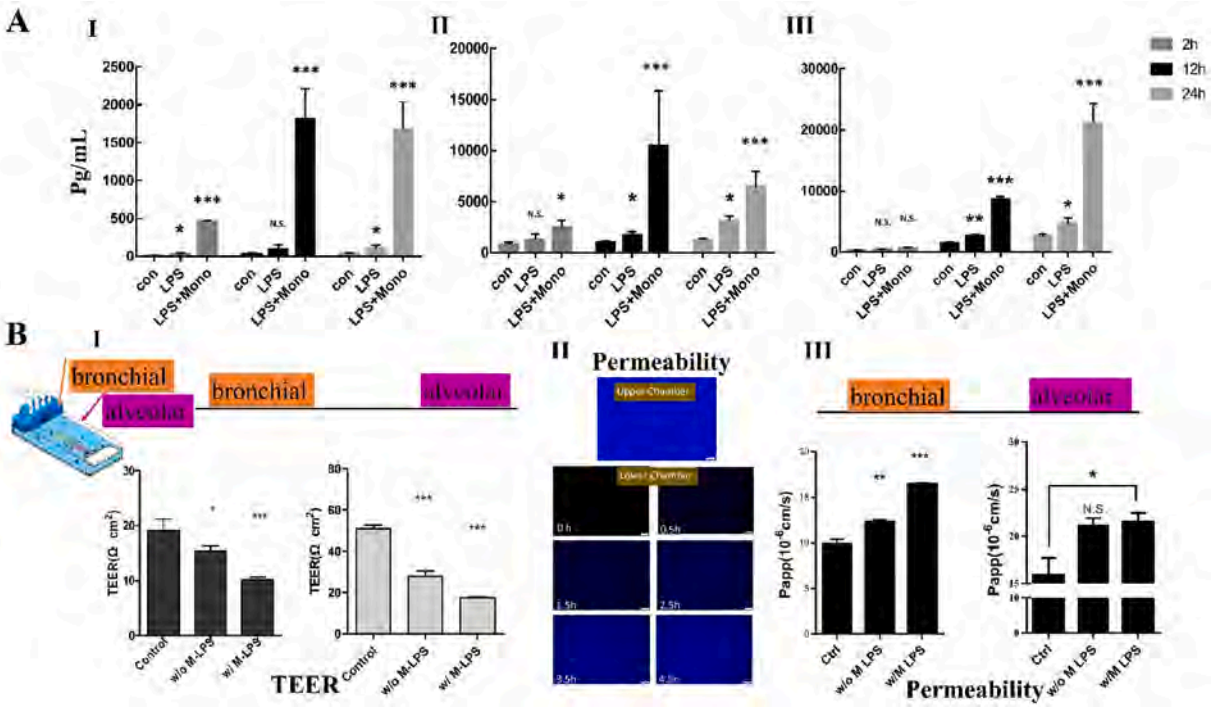

Fig. 3. Measurement of Inflammatory Reactions in the Lung-MPS. A) Inflammatory material cytokine secretion in the Lung-MPSs under different conditions. (I) TNF-α, (II) MCP-1, and (III) IL-6 (pg/ml). B) (I) TEER value measured in Lung-MPS bronchial and alveolar chambers, (II) permeability measured in Lung-MPSs showing the transfer of small fluorescence molecules from upper chamber to lower chamber against time, (III) the calculated permeability in bronchial and alveolar chamber under different conditions, where w/o M LPS means treatment without macrophages but with LPS. Data were compared with 6 samples in each group from three experiments. Significance was calculated by one-way ANOVA with Tukey's post-hoc tests. *$p < 0.05$, ***$p < 0.001$. N.S., no significance.

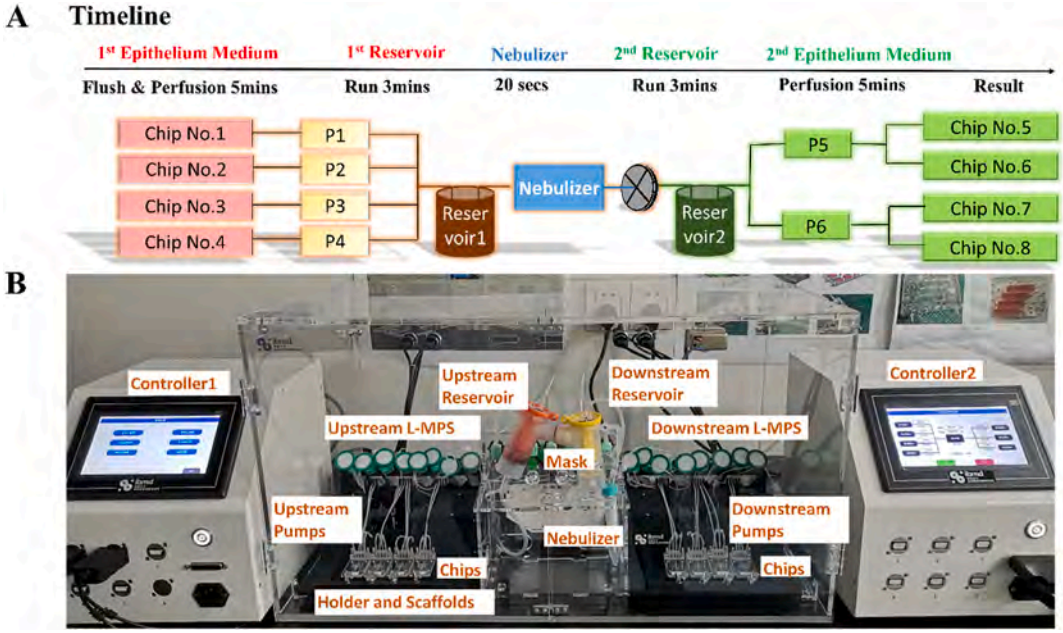

Fig. 4. Integrated Lung-MPSs for Spreading of Virus Particles. A) Illustrations and photographs of an integrated Lung-MPS system for a simulation of the droplet spreading between human lungs: Upper panel, timeline of the operation of the spreading system, Lower panel, diagram showing the components of the system. B) Photos of Lung-MPS, including: two control systems, upstream chips and pump systems, nebulizer, "mask", upstream and downstream reservoirs, downstream chips and pump systems.

3.5. Counting attached leukocytes and epithelial morphological analysis using artificial intelligence

Lung-MPS contains multiple flow chambers, different layers and multiple tissues, resulting in a complexity in imaging and a reduction in image quality. To better quantify the inflammation-induced changes in pulmonary epithelial cells and macrophages, we developed deep-learning-based algorithms to classify the status of these epithelial cell layers with macrophages attached. We used a model of the VGG-19 Network (Materials and Methods) trained by an existing training set to

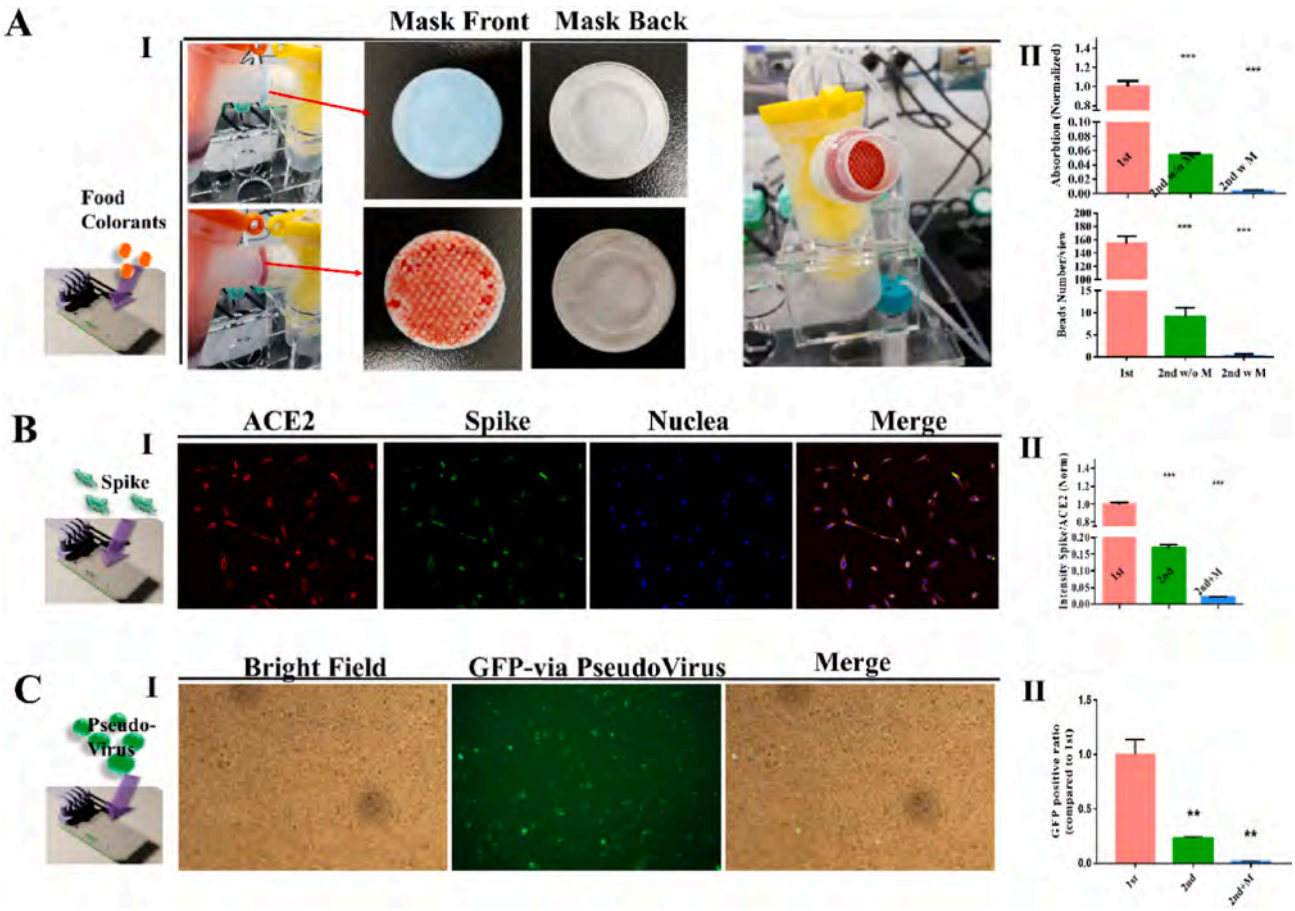

Fig. 5. Characterize the Spreading of Spike-Protein and Pseudo-Virus Particles in L-MPS. A) Food colorants and fluorescent microbeads were used to demonstrate the diffusion of small molecules or substances from the upstream cascade to the downstream cascade. The medium from the first Lung-MPS was nebulized and spread to the downstream Lung-MPS, with or without protection by pieces from surgery face masks. The right panel shows the spreading efficiency w/o and with masks. B) Fluorescence measurement of the spike protein and ACE2 colocalization. The spreading of the spike proteins was significantly attenuated by piece of masks measured by the fluorescence intensity decreased over 99% percent compared with the unmasked group. C) Pseudovirus in Lung-MPS. Live cell images were obtained at 12 h after infection. Cells with fluorescence signals above the threshold were obtained and counted automatically. In the first Lung-MPS, an average of 74 cells per microscopic view were found to be infected with GFP-labeled pseudovirions; in the second Lung-MPS, an average of 6 cells per view were recorded, while in the mask-blocked group, an average of less than one cells per view were recorded. Data were compared with 15–20 samples in each group from three experiments. Significance was calculated by one-way ANOVA with Tukey's post-hoc tests. $*p < 0.05$, $***p < 0.001$. N.S., no significance.

predict whether it is the normal (unstimulated) epithelium (Fig. 6A, left panel). A VGG network model used by the system is shown in Fig. 6A, (right panel). In brief, this network takes the preprocessed image with a size of 224 × 224 as input and outputs the predicted label (control and stimulation groups). The first two convolution groups have 2 convolution layers with 64 and 128 feature maps. The remaining three convolution groups contain 4 convolution layers with feature maps of 256, 512, and 512. The first two fully connected layers have 4096 channels each, and the third performs 2-way experimental condition classification and thus contains 2 channels (one for each class). The output was two states that represent the control (w/o stimulation) condition or the abnormal (w/stimulation) condition, as demonstrated in Fig. 6B. Both fluorescence and bright field images were tested, and the image with the best result was used. The accuracy of the model continuously improved as the number of training sessions increased (Fig. 6C). After 90 training epochs, its accuracy rapidly increased to above 0.9 (compared to ground truth), indicating its accuracy>90%.

We also applied an integrated learning method to increase the performance of our model. Considering that a real sample consists of four cell type (macrophages, epithelium, monocyte, endothelium) images, a 2-branch-VGG or 4-branch-VGG network was proposed that takes all four kinds of images as input and predicts the label of the sample by comprehensive analysis. The architecture of our network is shown in Fig. 3D. Each input image is first sent into a pretrained VGG19 feature extractor for deep feature extraction, and then the features of the four branches are concatenated for feature fusion. Finally, three fully connected layers are applied as the classifier. The 4-branch VGG network outputs two statuses representing two conditions. Because of the integrated learning strategy, the accuracy and loss curves of the model converge quickly (Fig. 6C). After 30 *epochs* (Materials and Methods), the accuracy of the training set reaches 99.8%, and the result on the test set is 97.9%, which increases considerably compared with the result of the previous VGG-19 network.

To test the capacity of our system, we applied stimulation in the 1st (upstream) and spread to 2nd (downstream) chips in MPS with or without masks (Fig. 6D). Three conditions were tested: control (PBS), LPS, pseudovirions, and the images in both bronchial and alveolar chambers where taken. The 4-branch VGG network deep-learning algorithms predicted the number of stimulated bronchial and alveolar tissues in the Lung-MPS, and the results are shown in Fig. 6E. Experiments were performed in six independent tests each time with four chips in each group. We found that LPS (10 μg/mL) can successfully activate both upstream and downstream Lung-MPSs while having a significantly reduced effect to mask protected Lung-MPSs, while masking completely protected the system from the virus infection considered. The Lung-MPS system in the LPS-mask protected group could not detect notable

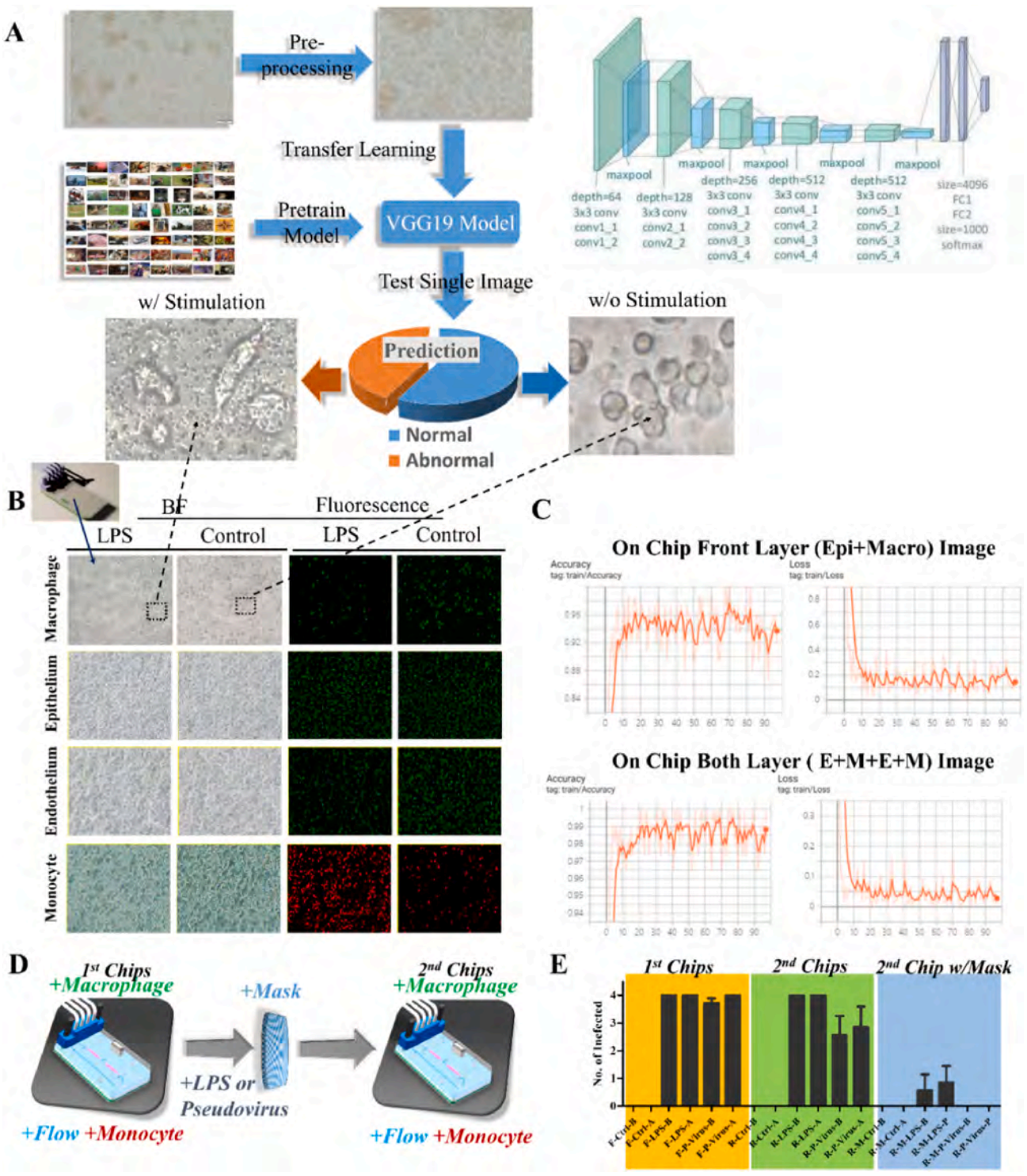

Fig. 6. Deep-Learning Based Algorism for Lung-MPS Activation Identification.A) Schematic illustration of the execution steps of the deep learning algorithm and the architecture of the VGG19 model used in this research. The VGG-19 network is composed of 5 convolution groups and 3 fully connected layers. All the convolution layers use a convolution kernel of 3 × 3, and there is a max-pooling layer at the end of each group. This network takes the preprocessed image with a size of 224 × 224 as input and outputs the predicted label (experimental group and control group). B) Examples of images of the macrophages, epithelium, endothelium and leukocyte inside of the L-MPS w/or w/o LPS treatment. C) Accuracy of prediction of Lung-MPS stimulation status as a function of rounds of training, evaluated by the F value. The accuracy increased when both layer (Epithelium + Macrophage + Endothelium + Monocytes) images were all analyzed together compared with the analysis of the front layer (Epithelium and Macrophages) only. D) The stimulation status was analyzed for both the 1st (upstream) and 2nd (downstream) chips in MPS, with or without masks. E) The Deep-Learning predicted the number of stimulated bronchial and alveolar tissues in Lung-MPSs with different treatments (Control, LPS, Pseudovirions) are shown in the diagram. Experiments were performed with four chips in each group in six independent tests.

inflammatory activation (by ELISA, or by experts, data not shown) but could be picked up by the deep-learning system, indicating the high sensitivity of the algorithm.

4. Discussion

Earlier lung OOC models have been applied for detecting bacteria, chemicals, and nanoparticles (Huh et al. 2010, 2012a). In this study, an MPS, with alveolar-and-pulmonary bronchus components and incorporating resident macrophages and patrolling monocytes was developed and applied to model the inflammatory cascade reaction and pseudovirus infection and spread. Because the MPS has independent alveolar and bronchial chambers, the permeability of the bronchi and alveoli and the release of mucus can be monitored independently. Some publications have introduced neutrophils into a lung-on-a-chip to investigate the immune reactions of diseases since lung inflammation is mediated at the organ-level(Benam et al., 2016; Nawroth et al., 2020). Based on these achivements and considering that monocyte/macrophage-mediated inflammatory storms play an important role in COVID-19 lung disease(Desterke et al., 2020), we constructed the MPS with macrophages and monocytes to observe inflammatory signals at the organ-level *in vitro*, and it truly exhibited enhanced inflammatory storm responses. Moreover, we fabricated the connected lung-MPSs and the liquid-atomization operating between the different groups of Lung-MPS. In the system, fluid perfusion, sampling and control of the chip are completely automated, and the on-off and flow rates of the fluid can be defined and regulated through user friendly software. The configuration of this integrated system permits the study of the spread of viruses and a comparison of the effects of various protective measures in a safe and automated way.

Our macrophage-containing Lung-MPS system is more sensitive for monitoring an inflammatory reaction. The ratio of macrophages to alveolar cells in the alveoli is generally approximately 1: 10 (Fig. 2). These resident macrophages act as sentinels in the immune system responding to bacteria, chemicals, dust, and other harmful agents (through PAMPs), or cell death (DAMPs). Because many OOCs or MPSs reported previously often lack this key component, they are deficient in generating the initial, but most effective, inflammatory signals. Thus, our Lung-MPS detects the existence of DAMPs or PAMPs produced by activated macrophages and virus particles (Figs. 2, 3 and 6) instead of relying on the inflammatory reaction generated entirely by epithelia or endothelia.

Furthermore, we demonstrated that the monocytes patrolling this MPS can lead to significantly elevated inflammatory signals. Initial inflammatory signals released by macrophages activate nearby endothelial cells, resulting in the expression of adhesion factors, such as I-CAM-1 and E-selectin, on endothelial cell surfaces(Libby and Luscher, 2020). Consequently, circulating monocytes introduced into our system may adhere, roll, and transmigrate through the endothelial layer. These accumulated monocytes generate inflammatory cytokines, resulting in local inflammation enhancement and leading to an increase in inflammatory signals (Figs. 2 and 3). These inflammatory cytokines could be responsible for the cytokine storm following SARS or COVID-19 infection; similar storms have been recapitulated in previous influenza *in vitro* model but without immune cells(Si et al., 2021b).

We demonstrated that the spike protein of SARS-CoV-2 can attach to the epithelium in our Lung-MPS, and the pseudovirus can infect the epithelium of Lung-MPS indicating that this system could be used for the study of infection by airborne pathogens that are contained in fluid droplets. Compared with a cell culture model, this model provides a more faithful representation of the biological situation in terms of cell-cell signaling and cell-matrix interactions and tissue functionality. Compared with an animal model, our model is composed of human cells and thus is better suited to study how disease spreads between people. The droplet spreading system we fabricated can be used for quantitatively studying viral infection in the lung-MPS and the effect of physical protective equipment (such as face masks) on the spread of the virus. This system also has potential applications in the study of viral spread among humans or from animals to humans or from humans to animals.

According to a previous study, there is a growing need to automate many biological *in vitro* experiments for improved accuracy, increased throughput, and reduced risk to researchers when working with pathogens or other laboratory hazards(Novak et al., 2020). Therefore, we constructed deep-learning based algorithms for analysis, which had an accuracy of above 93% (w/two images), and above 99% (w/four images) to evaluate the influence of viruses on the epithelia, macrophages, endothelia, and monocytes by imaging. As the complexity in the Lung-MPS structure reduced the imaging quality of each tissue, the morphological changes of each cell were not significant, even as judged by professional biologists. However, with the deep-learning algorithms, the program could distinguish the distinct differences in the images from control and stimulated Lung-MPS performing this classification task better than trained humans and with improved safety – everything was on chip and could be monitored remotely and fully automated.

5. Conclusion

In summary, we have developed a multichamber, multicell-component human Lung-MPS to monitor viral infection. For the first time, to our knowledge, we introduced resident macrophages and circulating monocytes in the system to simulate and study the inflammatory cascade in the lung. Using our MPS, changes in lung functions, such as the permeability of the Lung-MPS, mucus secretion, and inflammation, can be monitored in real time. We also developed deep-learning algorithms that can be applied in this Lung-MPS research to distinguish the morphological changes of epithelium, macrophages, and endothelium in Lung-MPS. Last, by introducing the SARS-CoV-2 spike protein and a SARS-CoV-2 pseudovirus, we demonstrated that this Lung-MPS could be employed to model pathological changes seen in COVID-19 patients and could also be useful for evaluating and screening drugs to ameliorate viral disease.

Funding

This work was supported by the National Key R&D Program of China (2017YFA0700500) and the Natural Science Foundation of Jiangsu province (Grant NO.BK20190192).

Author contributions

Z.C., J.H., J.Z., F.W., Z.W. and Q.L. performed all experiments. Z.C., J.C., Y.P., and Z.G. designed the project and wrote the manuscript. Y.Y, S.S., J.O, H.Y, J.G. developed and produced the hardware and software of the Lung microphysiological system. Z.C., Z.X., J.C., Y.P. and Z.G. contributed to manuscript editing and data analysis.

Declaration of competing interest

The authors declare that they have no known competing financial interests or personal relationships that could have appeared to influence the work reported in this paper.

Data availability

No data was used for the research described in the article.

Acknowledgments

We thank Prof. Ken Jacobson from University of North Carolina at Chapel Hill for critical input and suggestions.

Appendix A. Supplementary data

Supplementary data to this article can be found online at https://doi.org/10.1016/j.bios.2022.114772.

References

Bao, L., Deng, W., Huang, B., Gao, H., Liu, J., Ren, L., Wei, Q., Yu, P., Xu, Y., Qi, F., Qu, Y., Li, F., Lv, Q., Wang, W., Xue, J., Gong, S., Liu, M., Wang, G., Wang, S., Song, Z., Zhao, L., Liu, P., Zhao, L., Ye, F., Wang, H., Zhou, W., Zhu, N., Zhen, W., Yu, H., Zhang, X., Guo, L., Chen, L., Wang, C., Wang, Y., Wang, X., Xiao, Y., Sun, Q., Liu, H., Zhu, F., Ma, C., Yan, L., Yang, M., Han, J., Xu, W., Tan, W., Peng, X., Jin, Q., Wu, G., Qin, C., 2020. Nature 583 (7818), 830–833.

Benam, K.H., Villenave, R., Lucchesi, C., Varone, A., Hubeau, C., Lee, H.H., Alves, S.E., Salmon, M., Ferrante, T.C., Weaver, J.C., Bahinski, A., Hamilton, G.A., Ingber, D.E., 2016. Nat. Methods 13 (2), 151–157.

Chan, J.F., Zhang, A.J., Yuan, S., Poon, V.K., Chan, C.C., Lee, A.C., Chan, W.M., Fan, Z., Tsoi, H.W., Wen, L., Liang, R., Cao, J., Chen, Y., Tang, K., Luo, C., Cai, J.P., Kok, K. H., Chu, H., Chan, K.H., Sridhar, S., Chen, Z., Chen, H., To, K.K., Yuen, K.Y., 2020. Clin. Infect. Dis. 71 (9), 2428–2446.

Chen, Z., Ma, N., Sun, X., Li, Q., Zeng, Y., Chen, F., Sun, S., Xu, J., Zhang, J., Ye, H., Ge, J., Zhang, Z., Cui, X., Leong, K., Chen, Y., Z, G., 2021. Biomaterials 272, 120770.

Chu, H., Chan, J.F., Wang, Y., Yuen, T.T., Chai, Y., Hou, Y., Shuai, H., Yang, D., Hu, B., Huang, X., Zhang, X., Cai, J.P., Zhou, J., Yuan, S., Kok, K.H., To, K.K., Chan, I.H., Zhang, A.J., Sit, K.Y., Au, W.K., Yuen, K.Y., 2020. Clin. Infect. Dis. 71 (6), 1400–1409.

Danku, A.E., Dulf, E.H., Braicu, C., Jurj, A., Berindan-Neagoe, I., 2022. Front. Bioeng. Biotechnol. 10, 840674.

Denning, N.L., Aziz, M., Gurien, S.D., Wang, P., 2019. Front. Immunol. 10, 2536.

Desterke, C., Turhan, A.G., Bennaceur-Griscelli, A., Griscelli, F., 2020. iScience 23 (10), 101611.

Huang, D., Liu, T., Liao, J., Maharjan, S., Xie, X., Perez, M., Anaya, I., Wang, S., Tirado Mayer, A., Kang, Z., Kong, W., Mainardi, V.L., Garciamendez-Mijares, C.E., Garcia Martinez, G., Moretti, M., Zhang, W., Gu, Z., Ghaemmaghami, A.M., Zhang, Y.S., 2021. Proc. Natl. Acad. Sci. U. S. A. 118 (19).

Huh, D., Leslie, D.C., Matthews, B.D., Fraser, J.P., Jurek, S., Hamilton, G.A., Thorneloe, K.S., McAlexander, M.A., Ingber, D.E., 2012a. Sci. Transl. Med. 4 (159), 159ra147.

Huh, D., Matthews, B.D., Mammoto, A., Montoya-Zavala, M., Hsin, H.Y., Ingber, D.E., 2010. Science 328 (5986), 1662–1668.

Huh, D., Torisawa, Y.S., Hamilton, G.A., Kim, H.J., Ingber, D.E., 2012b. Lab Chip 12 (12), 2156–2164.

Jing, Y., Run-Qian, L., Hao-Ran, W., Hao-Ran, C., Ya-Bin, L., Yang, G., Fei, C., 2020. Mol Hum Reprod.

Libby, P., Luscher, T., 2020. Eur. Heart J. 41 (32), 3038–3044.

Low, L.A., Mummery, C., Berridge, B.R., Austin, C.P., Tagle, D.A., 2021. Nat. Rev. Drug Discov. 20 (5), 345–361.

Low, L.A., Tagle, D.A., 2017. Exp. Biol. Med. (Maywood, NJ, U. S.) 242 (16), 1573–1578.

Marcel, S., Rodriguez, Y., 2010. Torchvision the machine-vision package of torch. In: International Conference on Multimedea, p. 1485.

Mehta, G., Hsiao, A.Y., Ingram, M., Luker, G.D., Takayama, S., 2012. J. Contr. Release 164 (2), 192–204.

Nawroth, J.C., Lucchesi, C., Cheng, D., Shukla, A., Ngyuen, J., Shroff, T., Varone, A., Karalis, K., Lee, H.H., Alves, S., Hamilton, G.A., Salmon, M., Villenave, R., 2020. Am. J. Respir. Cell Mol. Biol. 63 (5), 591–600.

Novak, R., Ingram, M., Marquez, S., Das, D., Delahanty, A., Herland, A., Maoz, B.M., Jeanty, S.S.F., Somayaji, M.R., Burt, M., Calamari, E., Chalkiadaki, A., Cho, A., Choe, Y., Chou, D.B., Cronce, M., Dauth, S., Divic, T., Fernandez-Alcon, J., Ferrante, T., Ferrier, J., FitzGerald, E.A., Fleming, R., Jalili-Firoozinezhad, S., Grevesse, T., Goss, J.A., Hamkins-Indik, T., Henry, O., Hinojosa, C., Huffstater, T., Jang, K.J., Kujala, V., Leng, L., Mannix, R., Milton, Y., Nawroth, J., Nestor, B.A., Ng, C.F., O'Connor, B., Park, T.E., Sanchez, H., Sliz, J., Sontheimer-Phelps, A., Swenor, B., Thompson 2nd, G., Touloumes, G.J., Tranchemontagne, Z., Wen, N., Yadid, M., Bahinski, A., Hamilton, G.A., Levner, D., Levy, O., Przekwas, A., Prantil-Baun, R., Parker, K.K., Ingber, D.E., 2020. Nat. Biomed. Eng. 4 (4), 407–420.

Pal, R., Bhansali, A., 2020. Diabetes Res. Clin. Pract. 162, 108132.

Pirola, C.J., Sookoian, S., 2020. Gastroenterology 159 (4), 1620–1621.

Si, L., Bai, H., Oh, C.Y., Jin, L., Prantil-Baun, R., Ingber, D.E., 2021a. Microbiol. Spectr. 9 (2), e0025721.

Si, L., Bai, H., Rodas, M., Cao, W., Oh, C.Y., Jiang, A., Moller, R., Hoagland, D., Oishi, K., Horiuchi, S., Uhl, S., Blanco-Melo, D., Albrecht, R.A., Liu, W.C., Jordan, T., Nilsson-Payant, B.E., Golynker, I., Frere, J., Logue, J., Haupt, R., McGrath, M., Weston, S., Zhang, T., Plebani, R., Soong, M., Nurani, A., Kim, S.M., Zhu, D.Y., Benam, K.H., Goyal, G., Gilpin, S.E., Prantil-Baun, R., Gygi, S.P., Powers, R.K., Carlson, K.E., Frieman, M., tenOever, B.R., Ingber, D.E., 2021b. Nat. Biomed. Eng. 5 (8), 815–829.

Simonyan, Karen., Zisserman, Andrew., 2015. Very Deep Convolutional Networks for Large-Scale Image Recognition. The 3rd International Conference on Learning Representations (ICLR2015). https://www.robots.ox.ac.uk/~vgg/research/very_deep/.

South, A.M., Diz, D.I., Chappell, M.C., 2020. Am. J. Physiol. Heart Circ. Physiol. 318 (5), H1084–H1090.

Stone, K.C., Mercer, R.R., Gehr, P., Stockstill, B., Crapo, J.D., 1992. Am. J. Respir. Cell Mol. Biol. 6 (2), 235–243.

Sunghee Estelle Park, A.G., 2019. Dongeun Huh. Science 364, 960–965.

Takeuchi, O., Akira, S., 2010. Cell 140 (6), 805–820.

Yang, Y., Gao, B., Hu, Y., Wei, H., Zhang, C., Chai, R., Z, G., 2021. Nanoscale 13 (18), 8614–8622.

Yu, J., Tostanoski, L.H., Peter, L., Mercado, N.B., McMahan, K., Mahrokhian, S.H., Nkolola, J.P., Liu, J., Li, Z., Chandrashekar, A., Martinez, D.R., Loos, C., Atyeo, C., Fischinger, S., Burke, J.S., Slein, M.D., Chen, Y., Zuiani, A., Lelis, F.J.N., Travers, M., Habibi, S., Pessaint, L., Van Ry, A., Blade, K., Brown, R., Cook, A., Finneyfrock, B., Dodson, A., Teow, E., Velasco, J., Zahn, R., Wegmann, F., Bondzie, E.A., Dagotto, G., Gebre, M.S., He, X., Jacob-Dolan, C., Kirilova, M., Kordana, N., Lin, Z., Maxfield, L. F., Nampanya, F., Nityanandam, R., Ventura, J.D., Wan, H., Cai, Y., Chen, B., Schmidt, A.G., Wesemann, D.R., Baric, R.S., Alter, G., Andersen, H., Lewis, M.G., Barouch, D.H., 2020. Science 369 (6505), 806–811.

Zheng, F., Fu, F., Cheng, Y., Wang, C., Zhao, Y., Gu, Z., 2016. Small 12 (17), 2253–2282.